

Magnetization and magnetization reversal in epitaxial Fe/Cr/Co asymmetric spin-valve systemsF. Brüssing,^{*} B. Toperverg,[†] K. Zhernenkov, A. Devishvili, and H. Zabel
*Department of Physics, Ruhr-University Bochum, 44780 Bochum, Germany*M. Wolff
*Division for Materials Physics, Uppsala University, 75120 Uppsala, Sweden*K. Theis-Bröhl
*University of Applied Science, An der Karlstadt 8, 27568 Bremerhaven, Germany*C. Wiemann, A. Kaiser, and C. M. Schneider
Institut für Festkörperforschung, Forschungszentrum Jülich GmbH, 52425 Jülich, Germany
(Received 23 December 2011; revised manuscript received 13 February 2012; published 8 May 2012)

We have investigated asymmetric Fe/Cr/Co/Cr superlattices with two magnetic layers of Fe and Co, which are different with respect to their magnetic properties: magnetization, coercivity, and magnetic anisotropy. The magnetic layers are weakly coupled via a mediating Cr spacer layer providing an antiferromagnetic alignment of adjacent layers. The magnetic structure of these spin-valve-like Fe/Cr/Co/Cr superlattices was analyzed from the remanent state up to saturation via polarized neutron scattering and polarized neutron reflectivity (PNR). Furthermore, the domain structure in remanence was imaged via polarized x-ray photoemission electron microscopy (XPEEM). This analysis reveals that the Co magnetization strongly affects the Fe domain structure, while the layer magnetization is collinear from the remanent antiparallel state up to the ferromagnetic saturation state. However, for certain Co layer thicknesses, the as-grown remanent state exhibits a noncollinear antiferromagnetic spin structure, which cannot be recovered after applying a magnetic field. However, the noncollinear structure is reproducible with freshly grown superlattices.

DOI: [10.1103/PhysRevB.85.174409](https://doi.org/10.1103/PhysRevB.85.174409)

PACS number(s): 75.60.-d, 75.70.Cn, 25.40.Dn

I. INTRODUCTION

Magnetic multilayers and magnetic superlattices of the type $[F/N]_{\times m}$ (F = ferromagnetic layer, N = nonferromagnetic layer, m = number of repeats) have strongly contributed to our present understanding of interlayer exchange coupling,¹ proximity effects,² quantum well states,³ and magnetoresistive properties.⁴ Since most of these phenomena can be studied with corresponding $[F/N/F]$ trilayers, the present interest in magnetic multilayers has declined somewhat.⁵ However, multiple repetition of basic structural units, e.g., F/N bilayers, into a stack may cause cumulative effects of aforementioned phenomena that are not observed in the corresponding trilayers. In addition, a periodic repetition of units promises to reveal new physical phenomena related to the multilayer or superlattice periodicity, such as complex periodic magnetic structures (for instance helimagnets⁶) or zone folding and mode splitting effects of spin waves in superlattices.⁷ In fact, magnetic Bragg peaks from the superlattice periodicity permit a detailed Fourier analysis of the magnetization profile in superlattices from which precise interface properties have been derived and magnetization profiles close to the Curie temperature have been analyzed.^{8,9}

In most of these cases, the superlattice structure $[F/N]_{\times m}$ consists of symmetrically repeating structural units. A new situation occurs in asymmetric superlattices $[F_1/N/F_2/N]_{\times m}$ with different ferromagnetic layers F_1 and F_2 . This opens up new degrees of freedom where the layers F_1 and F_2 may differ with respect to their Curie temperature, composition, coercivity, anisotropy, domain size, etc. For instance, if the coercivities of the layers F_1 and F_2 are different, an

antiparallel alignment of the layers can be achieved between their respective coercive fields H_{c1} and H_{c2} without the need of an antiferromagnetic interlayer exchange coupling. Such systems may lead to a considerable simplification in the design of spintronic devices for magnetic data storage.

A combination of Fe and Co as magnetically soft and hard layers, respectively, separated by either insulating or nonmagnetic spacer layers are considered as key candidates for those devices. Among a number of reports existing in the literature, two examples may be mentioned that refer to pseudospin-valve trilayer Co/MgO/Fe (see Ref. 10) and the quadrolayer Fe/Cr/Au/Co revealing an inverse giant magnetoresistance effect.¹¹

Here, we report about investigations of $[\text{Co/Cr/Fe/Cr}]_{\times 20}$ epitaxial superlattices. In these superlattices, the coercivity of Co is rather large compared to the one of Fe. Therefore one can expect that the magnetization reversal in the Fe layers occurs at external fields that may not yet alter the magnetization in the Co layers. Such an expectation is based on the assumption that for sufficiently thick spacers, Fe and Co layers are magnetically uncoupled and react individually on the applied field. This is, however, not always the case and as-prepared magnetic configurations of multilayers may irreversibly be modified via external field application, as reported for some other systems.¹²⁻¹⁴ In our superlattices, the zero field as-grown state reveals a noncollinear magnetization configuration, which presumably results from the adjustment of magnetization directions in each consecutively deposited layer to stray fields generated by a set of domains in all previously deposited layers. The resulting metastable depth

profile and lateral domain configuration cannot be recovered after saturation, but can be reproduced with a new set of samples. Such noncollinear configurations were revealed by polarized neutron reflectivity and would have remained unnoticed by other methods. Furthermore, we investigate how Cr spacer layers influence the Co layer magnetization¹⁵ and how Fe and Co domains affect each other via magnetic coupling through the mediating Cr layer. Coupling of the magnetic layers in spin valve systems was already suspected for other systems studied by polarized neutron reflectivity.^{16,17} Here, we give a detailed account of the coupling by varying the mediating Cr layer thickness.

In the present study, we address the influence that the reversal of one type of layers has on the other type of layers in the superlattices $[\text{Co}/\text{Cr}/\text{Fe}/\text{Cr}]_{\times 20}$ and how the domain structure in both types of layers is altered by proximity effects. For this purpose, we have investigated the as-grown state and the magnetization reversal in real and reciprocal spaces. For the analysis of the layer magnetization and domain structure, we used specular and off-specular polarized neutron reflectivity measurements (PNR). In addition, we have imaged the domain structure by photoemission electron microscopy (PEEM) with resonant and circular polarized incident soft x rays. The present study amends earlier investigations of Co/Cr/Fe trilayers via the magneto-optic Kerr effect (MOKE).^{18,19} In these previous studies, we have established the range of interlayer exchange coupling between Fe and Co layers across the mediating Cr layer¹⁸ and the magnetization reversal process of single Fe and Co layers as compared to the coupled layers using vector MOKE.¹⁹ Before we discuss our present results in Secs. IV, VI, and V, we first describe the sample preparation of the superlattices in Sec. II and x-ray structural characterization in Sec. III. The experimental results are discussed in Sec. VII.

II. SAMPLE DESIGN AND PREPARATION

$[\text{Cr}/\text{Co}/\text{Cr}/\text{Fe}]_{\times 20}$ superlattices were prepared via molecular beam epitaxy (MBE) on a MgO(001) single-crystal substrate.¹⁸ The layer sequence of the superlattice is schematically shown in Fig. 1. For good epitaxial layer-by-layer growth, a ~ 60 -nm-thick Cr(001) buffer layer was first deposited on the MgO(001) substrate at a substrate temperature of 450 °C. The crystallinity of the Cr buffer layer was significantly improved by postgrowth annealing at a temperature of 750 °C for 5 min. During the growth of the superlattice, the substrate temperature was lowered to 300 °C as a compromise between good epitaxial growth and suppression of interdiffusion of the layers. The

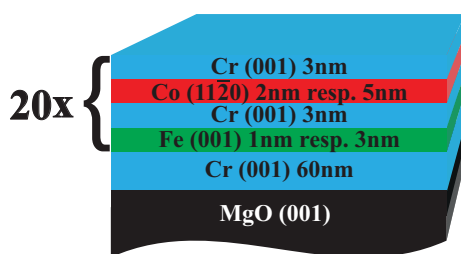


FIG. 1. (Color online) Layer sequence of the $[\text{Co}/\text{Cr}/\text{Fe}/\text{Cr}]_{\times 20}$ superlattice.

TABLE I. Atomic layer distances for the observed Bragg peak positions. d_{SL} refers to the average atomic layer distance in the superlattices.

	Sample I (10 nm)	Sample II (16 nm)
d_{Co}	0.129 ($a = 0.364$)	0.127 ($a = 0.360$)
d_{Cr}	0.144 ($a = 0.289$)	0.144 ($a = 0.289$)
d_{SL}	0.137 ($a = 0.137$)	0.138 ($a = 0.138$)

epitaxy of Fe on Cr is pseudomorphic because of a lattice misfit of only 0.6% between both bcc materials. In contrast, the growth of Co in such a system is more complex.²⁰ Co grows in a (11 $\bar{2}$ 0) orientation on Cr(001) with $\text{Co}[0001] \parallel \text{Cr}[110]$. This results in pseudomorphic growth of Co on Cr with a 45° epitaxy and lattice misfits of 0.07% parallel to $\text{Co}[0001]$ and 6.4% parallel to $\text{Co}[1\bar{1}\bar{2}0]$. Because of the two equivalent [110] in-plane axes in Cr(001), different $\text{Co}(11\bar{2}0)$ domains form with an angle of 90° to each other.²¹ In addition to this, a bcc-hcp structural phase transition takes place as a function of Co thickness within a thickness range of 0 nm (bcc) up to 4.0 nm (hcp).^{20,21} The Cr interlayer thickness between Co and Fe was chosen to be 3.0 nm, which mediates a weak antiferromagnetic (AF) coupling as reported in Ref. 18. Furthermore, we have chosen different thicknesses for the Co and Fe layers in order to cancel out the film net magnetization, whenever the magnetization orientation of Co and Fe are antiparallel. More details of the sample growth conditions can be found in Ref. 19.

We have prepared a total of ten superlattices with the same layer sequence and the same number of repetitions (20), but with different nominal thicknesses of the magnetic layers under identical conditions. In the first set of four superlattices with a periodicity of 10 nm, the thicknesses are 3, 3, 1, and 3 nm for the Co, Cr, Fe, and Cr layers, respectively. We will refer to this first set as *10-nm superlattice*. In the second set of six superlattices with a periodicity of 16 nm, the nominal thicknesses are 7, 3, 3, and 3 for the Co, Cr, Fe, and Cr layers, respectively. The second set is referred to as *16-nm superlattice*. Note that in the second set of superlattices, the magnetic layer thicknesses are doubled compared to the first set. The layer thicknesses according to x-ray analysis and fit are discussed in the next section and are listed in Table II.

For the structural analysis with x-ray scattering, we used the diffractometer W1.1 at the wiggler beam line of the HASYLAB at DESY in Hamburg, Germany. Polarized neutron reflectivity (PNR) measurements were taken using the neutron reflectometers ADAM^{22,23} and Super ADAM at the Institut

TABLE II. Thicknesses in nanometers of the layers in both superlattices according to fits to the reflectivity curves. The label (10 nm) and (16 nm) refers to nominal periodicities of the superlattices. t_{SL} is the periodicity of the superlattices.

t [nm]	Sample I (10 nm)	Sample II (16 nm)
t_{Co}	2.7 ± 0.1	7.4 ± 0.2
t_{Cr}	2.4 ± 0.1	2.5 ± 0.1
t_{Fe}	1.4 ± 0.1	3.0 ± 0.1
t_{Cr}	2.7 ± 0.1	2.8 ± 0.1
t_{SL}	9.4	15.7

Laue-Langevin, Grenoble, France.²⁴ The photoemission electron microscopy (PEEM) experiments were carried out at BESSY II of the Helmholtz Zentrum Berlin using a modified FOCUS IS-PEEM.²⁵

III. STRUCTURAL CHARACTERIZATION

The structural quality of the $[\text{Co/Cr/Fe/Cr}]_{\times 20}$ superlattices was checked using hard x-ray scattering in the small-angle regime via x-ray reflectivity measurements (XRR) and via high-angle x-ray diffraction (XRD).²⁶ XRR accesses the layer thicknesses, the interface roughness, and the correlation function parallel and perpendicular to the layers.^{27,28} Additionally, XRD provides data on the crystalline structure of the individual layers, their epitaxial relationship, and their strain state. Furthermore, transverse scans in the epitaxial plane and perpendicular to it yield information on the mosaic spreads and grain size.²⁹

For XRR measurements, we tuned the x-ray wavelength to near the Fe K_{α} -edge at 7.1 keV in order to increase the x-ray optical contrast between Fe and Cr layers. Figure 2 shows the specular reflectivity of two samples, one with a periodicity of 10 nm (bottom panel) and the other one with a periodicity of 16 nm (top panel). In both cases, quite a number of superlattice Bragg peaks can be recognized, indicative of a well defined periodicity and sufficiently sharp interfaces. At the same time, Bragg peaks become heavily suppressed at higher reflection angles indicating the influence of the interface smearing due to, e.g., appreciable interfacial roughness. The Bragg peaks are superposed by Kiessig fringes,³⁰ which are due to the 60-nm-thick Cr buffer layer. The solid lines through the data points represent the best fit,³¹ yielding the structural parameters listed in Table II.

A map of the specular reflected intensity and the diffuse scattering is reproduced in Fig. 2 (top inset). The specular ridge runs from the bottom left part of the map to the top right part. At the positions of the Bragg peaks, streaks of diffuse scattering are visible, which emanate in the direction perpendicular to the specular reflectivity ridge. In the bottom left part of the map, the effect of the Yoneda scattering is quite pronounced. Without detailed analysis, from the intensity and shape of the diffuse scattering in the map, one can immediately state that the in-plane correlation length is quite short and in the perpendicular direction, comprises only a few repeats. The inset in the bottom panel of Fig. 2 shows two line scans of the off-specular diffuse scattering, taken at the position of the second Bragg peak and at the minima in front of fourth Bragg peak. These scans also indicate weak intensities from low and uncorrelated roughness.

Next we turn our attention to the crystal structure, which was analyzed by XRD at an x-ray energy of 11 keV. With the higher energy, the penetration depth was enlarged as compared to the XRR experiments. The top graph in Fig. 3 shows the out-of-plane diffraction pattern in the region of interest for both samples (red 10 nm and black 16 nm) covering the substrate MgO(002) Bragg peak, the bcc Fe/Cr(002) peak, and the hcp Co(11 $\bar{2}$ 0). The relevant peak positions are listed in Table I. For both samples, the position and shape of the Fe/Cr peak is identically. The Co peak is at $Q = 48.8 \text{ nm}^{-1}$ for the 10-nm sample and at $Q = 49.3 \text{ nm}^{-1}$ for the 16-nm sample. The shift

of this position is related to the relaxation of the bcc lattice $Q = 44.6 \text{ nm}^{-1}$ (see Ref. 32) to the hcp lattice $Q = 50.1 \text{ nm}^{-1}$. The values reveal a system that is not completely relaxed to the hcp structure.²⁰ In addition, a fundamental Bragg reflection from the average lattice parameter of all constituent layers can be observed at $Q = 45.9 \text{ nm}^{-1}$ (10 nm) and $Q = 45.4 \text{ nm}^{-1}$ (16 nm), the shift of this peak being related to the different contributions of the Fe/Cr and the Co peaks in both cases. In combination with the also visible Laue oscillations, the superlattice periodicities of 10 nm and 16 nm are confirmed.

The epitaxial relationship and domain structure was determined by rocking scans in the azimuthal plane using surface scattering geometry, i.e., rotating the sample under the condition of glancing angles of incident and scattered x-ray beams close to total reflection, such that the scattering vector is in the film plane. Figure 3 bottom panel shows the results for both samples and for different Bragg peaks from the different layers in the superlattices. We notice a four-fold orientational dependence of the MgO(200) Bragg peak intensity, as expected. In relation to the MgO Bragg peaks,

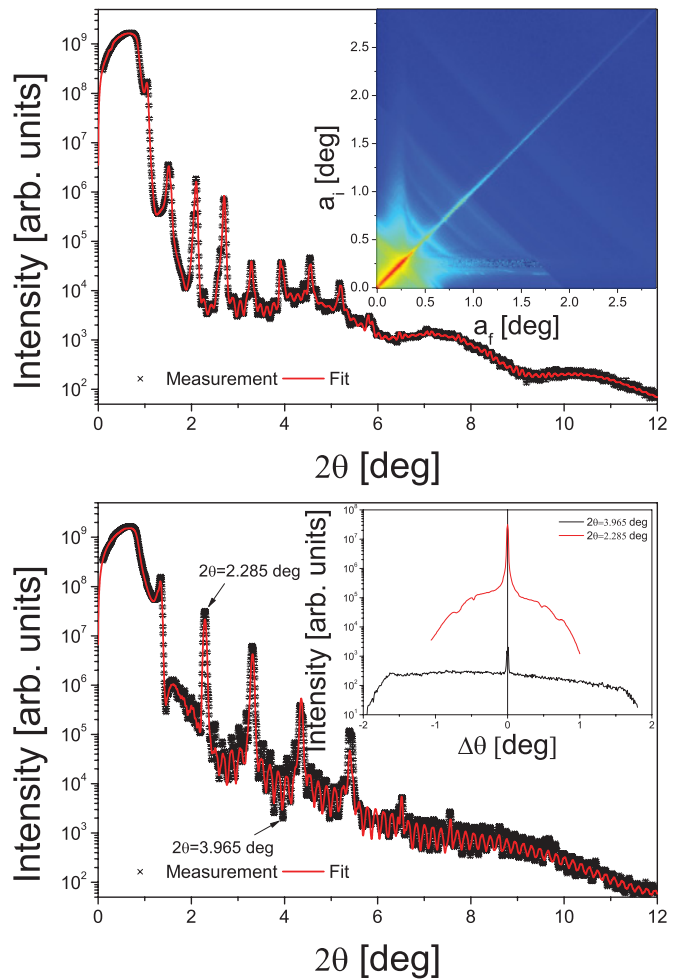


FIG. 2. (Color online) Reflectivity measurement of two superlattices with nominal periodicities of 16 nm (top panel) and 10 nm (bottom panel). The inset in the top panel shows a map of specular and off-specular scatterings, the inset in the bottom panel reproduces two off-specular scans taken at the 2θ position of the second and fourth Bragg reflections.

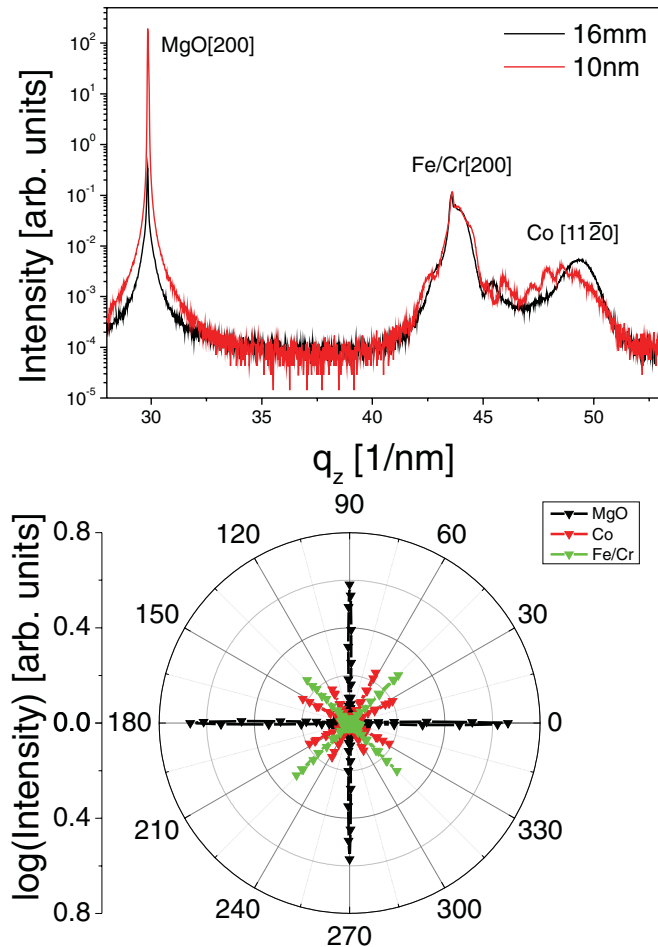


FIG. 3. (Color online) Top: measurement of the out-of-plane epitaxial relations 10-nm (red) and 16-nm (black) periodicities. Bottom: in-plane epitaxial relations for the MgO substrate, Fe/Cr, and Co layers in the superlattices with periodicities of 10 nm and 16 nm.

the Cr(200) peaks are rotated by 45° . These peaks originate mainly from the Cr buffer layer and cannot be distinguished from the Fe/Cr layers in the superlattice. The relative position of the peaks are listed in Table III.

Interesting is the azimuthal orientation of the hcp-Co($\bar{1}\bar{1}01$) and the bcc-Co(011) peaks that have nearly the same lattice

TABLE III. Relative azimuthal peak positions of MgO(200), Fe/Cr(200), and Co ($\bar{1}\bar{1}01$) layers for both superlattices with periodicities of 10 nm and 16 nm. The “'” is used to distinguish between different domains.

$\Delta\phi$	Sample I (10 nm)	Sample II (16 nm)
MgO (020)	0	0
MgO (002)	90	90
Fe/Cr (020)	45	45
Fe/Cr (002)	135	135
Co ($\bar{1}\bar{1}01$)/ Co (011)	27.17	27.67
Co ($\bar{1}\bar{1}01$)/ Co' (011)	62.67	62.67
Co' ($\bar{1}\bar{1}01$)/ Co (01 $\bar{1}$)	117.17	117.17
Co' ($\bar{1}\bar{1}01$)/ Co' (01 $\bar{1}$)	152.67	152.17

parameters. In both cases, all eight measured peaks refer to two crystal subdomains, which are turned by 35° (bcc-Co) or by 90° (hcp-Co) with respect to each other. The magnetic easy axis for the Co bcc lattice is $[001]$. From the measured peak positions, we can calculate that this axis is turned by 17.8° with respect to the easy axis of Fe. During the bcc-hcp transition, also the direction of the easy axis of Co changes to the c axis of the hcp-Co, which is parallel to one of the easy axes of Fe. In both cases, both Co crystalline domains result in an average fourfold anisotropy with easy axes parallel to the Fe easy axes.

IV. MAGNETIC CHARACTERIZATION VIA MOKE

The magnetic characterization of our samples was done using a magneto-optic Kerr effect (MOKE) apparatus and a SQUID magnetometer. For the MOKE measurements,³³ samples were prepared under the same conditions as for the superlattices, however, containing only one repeat unit. This is sufficient for MOKE measurements and, furthermore, saves the superlattices for later PNR work on the pristine state of the samples. In the following, we will call them 10-nm and 16-nm equivalent samples. The hysteresis loops parallel to the easy axis for both trilayers are shown in Fig. 4 (top panel). In both cases, the hysteresis consists of two overlapping loops for Fe with a very small coercive field and for Co with a much larger coercive field. Furthermore, the Co coercive fields for both samples are vastly different with 100 mT for the 10-nm equivalent sample (red) as compared to 220 mT for the 16-nm equivalent sample (black). This difference is related to the different Co layer thicknesses in both samples, which are 2 nm and 7 nm, respectively. The thickness of the Co layer is crucial as for increasing thickness a bcc-hcp structural phase transition takes place, as already alluded to in the previous section. We believe that this structural phase transition is responsible for the coercive field values observed. Some more details on the magnetic behavior of this system can be found in Ref. 19.

We have also measured the magnetic hysteresis of both superlattices *a posteriori* to the PNR experiments using MOKE and a SQUID magnetometer. The results are shown in Fig. 4 (bottom). For a detailed data analysis, we assume that the hysteresis loops are composed of two different and almost independent hysteresis loops for the Fe and Co layers, respectively. A step function, which can describe the shape of the hysteresis, is used to separate these two contributions for the MOKE and the SQUID data. Two representative examples for this analysis are shown in the insets of Fig. 4 (bottom). Then the SQUID data served to normalize the extracted and individual MOKE hysteresis loops for Co and Fe. These separated and normalized hysteresis loops are then used to calculate the reversal energy defined by the enclosed area of the hysteresis as a function of the azimuthal angle, see Fig. 5. From the azimuthal dependence of the reversal energy for each individual layer, we can conclude that the easy axis of the Fe and Co layers are at 45° and 135° , which is equivalent to the $[100]$ direction of Fe and the $[0001]$ direction of Co. The spikes that appear for the 16-nm sample at 45° and 135° are related to a nearly perfect alignment of the field along the easy axes of the sample. The small torque, which is then applied to the magnetic moments, results in an increase of the reversal energy.

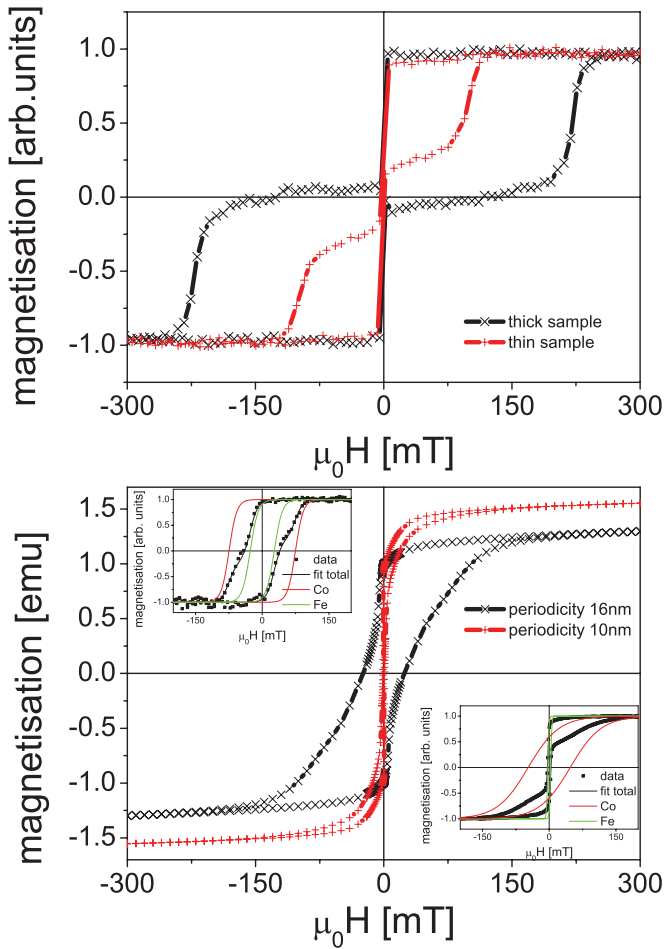


FIG. 4. (Color online) Top: hysteresis loops for trilayer samples similar to the 16-nm sample (black) and the 10-nm (red) superlattices measured by MOKE. Bottom: hysteresis loops measured with SQUID for the 16-nm (black) and 10-nm (red) sample equivalent to the respective superlattices. The insets demonstrate the data analysis of MOKE data for the individual Fe and Co layers (top left, 16 nm and bottom right, 10 nm).

The comparison of the reversal energy for Fe and Co shows some surprising results. For the 16-nm sample, the reversal of Fe and Co requires roughly the same energy, but in the case of the 10-nm sample, the required energy is by a factor of ten smaller for the Fe layer. We conclude from this fact that in the case of the 16-nm sample, the reversal of the Fe layer is dominated by the reversal of the Co layer. In case of the 10-nm sample, the reversals of the Co and Fe layers are independent from each other resulting in different energies for the reversal of both layers.

V. MAGNETIC CHARACTERIZATION VIA PNR

A. Saturation

Now we turn our attention to the PNR measurements. Before discussing the most interesting results for the as-grown state (see Fig. 6), as a reference, and then measurements in the plateau region (Fig. 8) of the hysteresis curve, between the magnetic field at which the Fe and Co layers switch. To saturate the

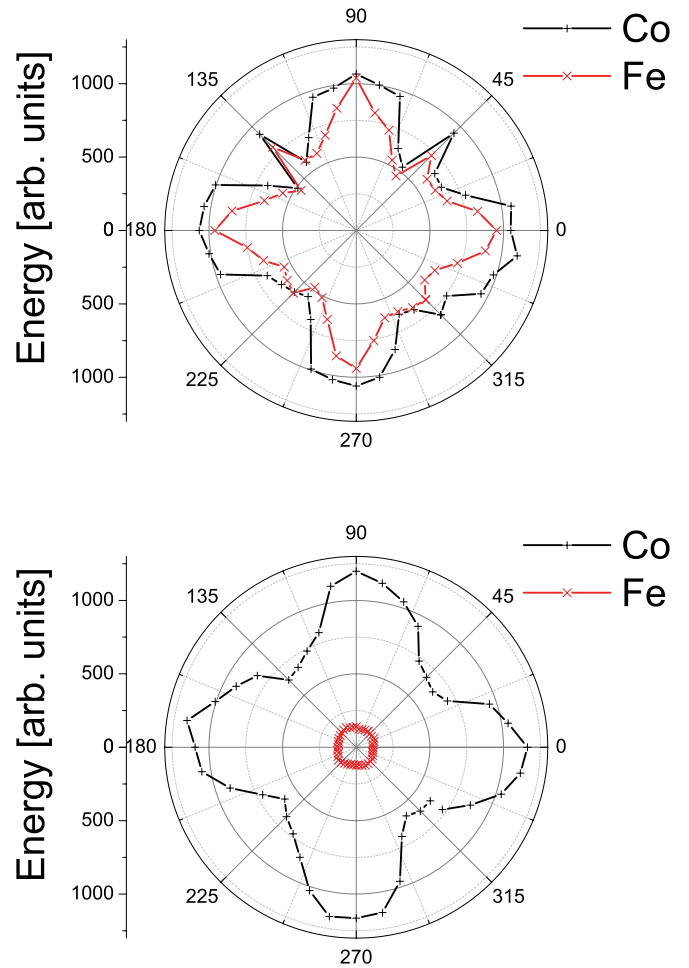


FIG. 5. (Color online) Reversal energy as a function of azimuthal angle for the individual Co and Fe layers in the superlattice with 16-nm periodicity (top) and for the superlattice with 10-nm periodicity (bottom). The reversal energy is determined from the area that the hysteresis encloses, after separating the combined hysteresis into individual hysteresis loops for Co and Fe, according to the insets in Fig. 4.

films an external field of 500 mT is applied perpendicular to the scattering plane, usually referred to as the Y direction.³⁴ In saturation, the magnetization is along the Y axis and it is sufficient to record the two polarized reflectivities R_U and R_D with initial neutron polarization parallel (up) and antiparallel (down) to the magnetic field, respectively. Then the chemical (nuclear) and the magnetization profile in the superlattice is deduced. The measurements and parameters extracted from the fitting are then kept fixed for the modeling of the magnetization profile in the plateau region and in the as-grown state. In the saturated state, the nuclear scattering length density (SLD) and the magnetic SLD profiles have the same periodicity resulting in a superposition of Bragg reflections for both polarization directions. However, due to the magnetic induction in the film the Bragg peaks have different intensities in R_U and R_D . The data for the 10-nm and 16-nm samples are shown in Fig. 6 together with the fit results.

The data for both R_U and R_D were fitted simultaneously by a theoretical model including the superstructure period, individual layer thicknesses, static Debye-Waller (DW) factors

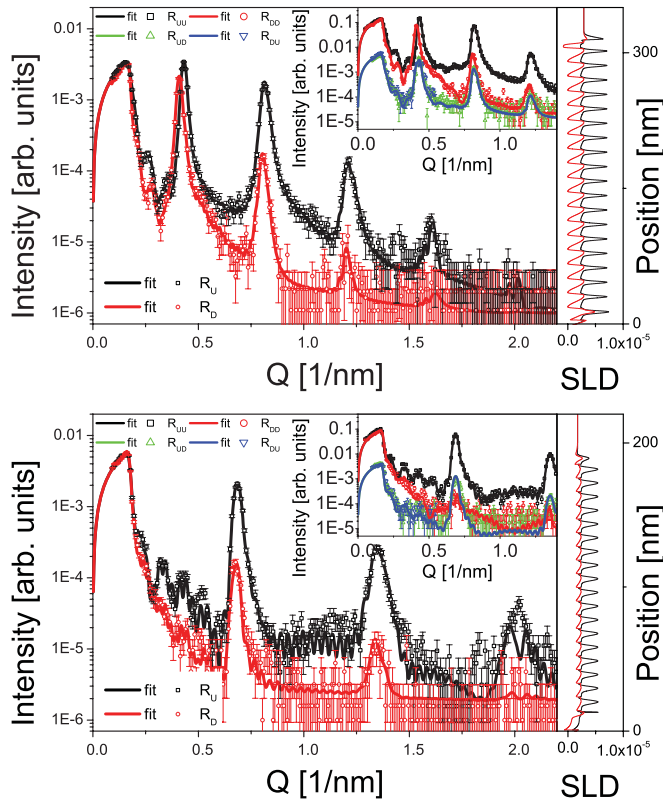


FIG. 6. (Color online) Polarized neutron reflectivity of the Co/Cr/Fe/Cr superlattices in the saturation state with parallel magnetization of the Co and Fe layers perpendicular to the scattering plane. Top panel: sample with a periodicity of 16 nm. Bottom panel: sample with a periodicity of 10 nm. On the right hand side of both graphs, the scattering length density profiles for spin-up polarized neutrons (black) and spin-down neutrons (red) are plotted.

describing the smearing of interfaces, as well as the mean values of the magnetic SLD of the Fe and Co layers.³⁵ For the fit, the nuclear SLDs were fixed to their reference values extracted from the saturated state. The fit result confirms the superlattice periods: 16.1(7) nm and 9.8(3) nm found from the fit of the x-ray data. The PNR fit also confirms an appreciable smearing of the interfaces causing a pronounced suppression of higher order Bragg reflections in Fig. 6. This interface smearing is found to be cumulatively increasing from the bottom to the top of the multilayers, reaching values that are comparable to the outermost layer thicknesses. The magnetic SLD of the Fe layers corresponds to the reference value for the saturation magnetization of 22 kG. In contrast, it turns out that the magnetization of the thicker and thinner Co layers is only half and one fourth of the reference value for the Co saturation magnetization of 18 kG, respectively. The SLD profile as a function of depth is plotted in Fig. 6 for both superlattices. One possible reason for the reduction of the Co moment is a canting of the Co magnetization vector with respect to the Y axis. A canted state, however, should result in neutron spin-flip scattering. Therefore additional PNR measurements with polarization analysis were carried out. For a canted state, the magnetization component normal to the quantization axis should flip the neutron spin. The experimental results along with the fit to the same model as above are displayed as insets

of Fig. 6. From these figures, it is clearly seen that no SF intensity is detected except the one resulting from the imperfect initial polarization and polarization analysis, both being about 96% versus 98.5% incident polarization reached in the former experiment.

This implies that the magnetization vector is indeed parallel to the applied field, but its absolute value is smaller than expected. Although a reduction of the Co magnetization in layers sandwiched between chromium was reported earlier in literature,¹⁵ the reason remains unclear. Possibly it is related to the conditions of coexistence of the uniaxial and cubic crystal phases of Co. Competing anisotropy of these two phases may induce the formation of small magnetic domains that cannot be erased with the fields that are normally sufficient for saturating bulk cobalt. The other possibility is magnetic roughness related to the structural roughness at the interfaces. In the latter case, different neighboring Co spin pairs may be exchange-coupled either directly, or via the chromium. This would result in a strongly frustrated spin state with substantial reduction or vanishing of the magnetization in the interface vicinity.

Lateral magnetic domains can be detected and “discriminated” from interfacial magnetic roughness via measurements of off-specular scattering. Therefore we have recorded the off-specular intensity using a position sensitive detector (PSD). The experimental result is represented in intensity maps plotted over the incident angle α_i and exit angle α_f of the neutrons with respect to the sample surface and for both incident spin states (up or down) (see Fig. 7) together with theoretical simulations carried out in the distorted wave Born approximation (DWBA)³⁶ for scattering from magnetic interfacial roughness. The high-intensity ridge running along the diagonal $\alpha_f = \alpha_i$ is the specular reflectivity. At the position of Bragg peaks, the specular ridge is crossed by Bragg sheets running perpendicular. A large extension of low-intensity Bragg sheets strongly suggests that lateral magnetic inhomogeneities are small. Moreover, their intensity strongly depends on the neutron spin state. Such a dependency arises of two facts. First, the two spin components of the neutron spin waves propagating in the mean magnetic potential have different amplitudes. This difference is, however, not sufficient to reproduce the magnitude of the spin asymmetry and a mechanism of spin-dependent scattering from lateral inhomogeneities has to be included. As is well known,³⁶ pure magnetic scattering, e.g., from domains, is quadratic with respect to magnetization deviations from the mean value. Therefore this is not the mechanism present here. On the contrary, the interference between magnetic and nuclear scattering is bilinear with respect to deviations of magnetic and nuclear potentials and hence brings spin-dependent contribution into the cross section of off-specular scattering. The only necessary condition for this effect is that both deviations are strongly correlated laterally. The correlations are automatically realized in the case of lateral fluctuations induced by interface roughness, which, in turn, produce lateral fluctuations of the nuclear SLD, with a domain size being on the order of only 30 nm.

B. Plateau region

Starting from negative saturation and following the ascending branch of the hysteresis loop, the magnetization vector

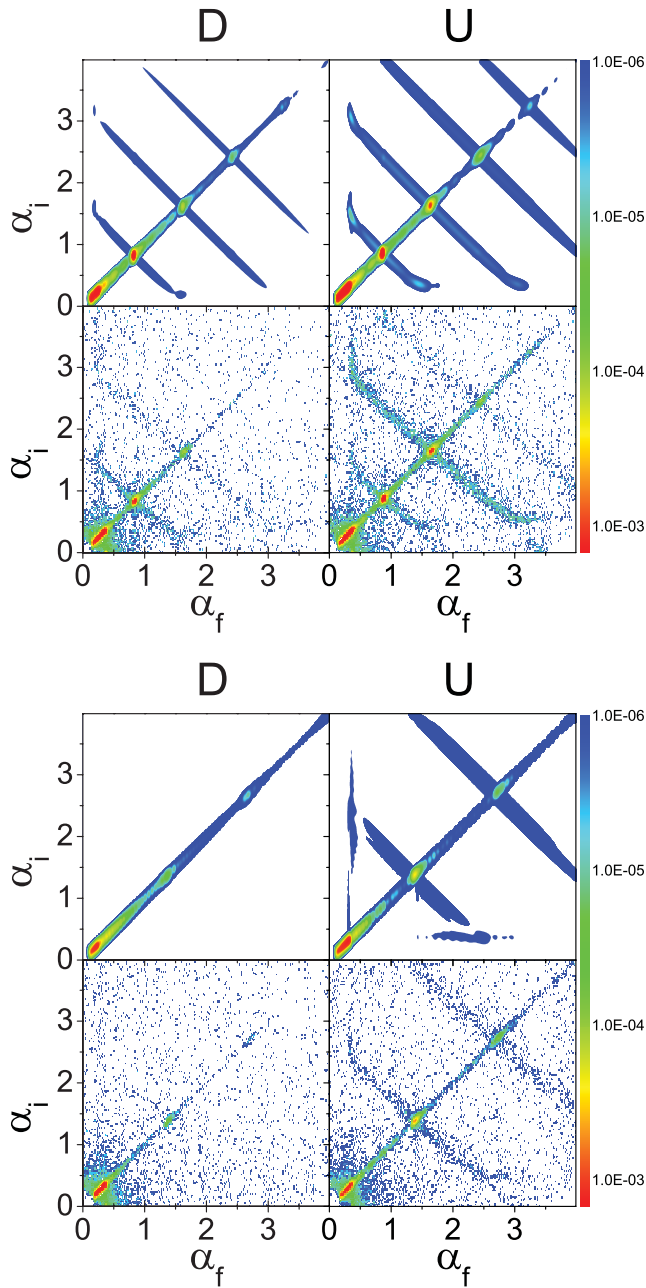


FIG. 7. (Color online) PNR maps for the saturated state of the 16-nm (top) and 10-nm (bottom) superlattices using spin-up and spin-down incident neutrons. The angles $\alpha_{i,f}$ (in degrees) refer to the neutron incident and final glancing angles to the sample surface, respectively. For each case, in the top row simulated maps are shown from which the magnetic domain size can be inferred to be on the order of 30 nm.

of the Fe layer flips into the field direction, whenever the applied field H exceeds the coercive field of Fe $H_{c,Fe}$. At the same time, within the field range $H_{c,Fe} \leq H \leq H_{c,Co}$, where $H_{c,Co}$ is the coercive field of cobalt, the magnetization vector of the Co layer should remain antiparallel to the applied field and to the magnetization vector of the Fe layer. Usually, in antiferromagnetic multilayers, the magnetic periodicity is doubled with respect to the chemical (nuclear) one. This leads

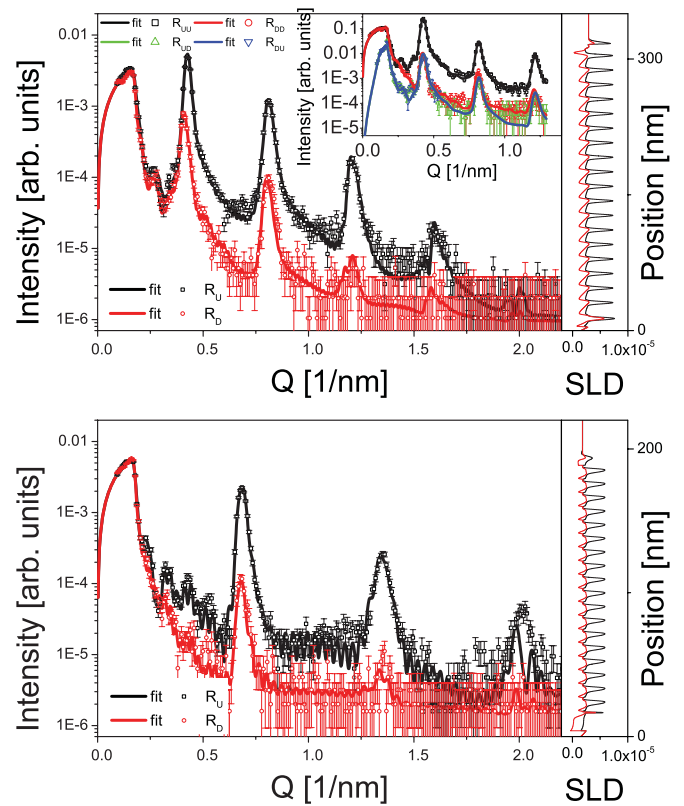


FIG. 8. (Color online) Polarized neutron reflectivity of the Co/Cr/Fe/Cr superlattices in an antiparallel state of the Co and Fe layers. Top panel: sample with a periodicity of 16 nm. Bottom panel: sample with a periodicity of 10 nm. On the right hand side of both graphs, the scattering length density profiles for spin-up (black) and spin-down (red) neutrons are plotted. The inset in the top panel shows PNR scans of all four cross sections.

to magnetic Bragg peaks at half order positions. However, in our more complex asymmetric [Co/Cr/Fe/Cr] superlattices, the chemical unit cell comprises already two different magnetic layers. Therefore irrespective of whether the magnetic layers are ferromagnetically or antiferromagnetically aligned, the structural and the magnetic periodicities remain the same. However, the magnetic splitting of the Bragg peaks should be different for parallel and antiparallel orientations as the magnetization profile is different. This is exactly what we observe in Fig. 8 for an external field of 50 mT, which is in the plateau region of both superlattices. The R_U and R_D reflectivities are distinctly different from those for the saturated state depicted in Fig. 6. The $R_{U/D,D/U}$ reflectivities are reproduced in the inserts and do not show spin-flip scattering either, aside from the one that is due to incomplete polarization and spin analysis.

One should, however, admit that differences between PNR curves in those two sets of figures do not yet guarantee antiparallel alignment of magnetization vectors in Fe and Co layers. Moreover, such a model does not quantitatively agree with the experimental data. Instead, a good fit of the PNR curves was obtained when releasing the magnetization values, but keeping all structural parameters fixed to those obtained from the fit of the PNR data taken for the saturated samples.

The fit results in a magnetization value for iron that agrees well with the nominal saturation value, but the magnetization of cobalt appears to be much smaller than previously determined in saturation. Further improvement of the fit was achieved via division of each cobalt layer into two sublayers with varying magnetization values. Such a procedure allows to mimic the magnetization depth profile within each layer. The core layer magnetization is found reduced to about the same value as previously found in saturation, while 2-nm interfacial layers are almost totally demagnetized. On the first sight, a loss of magnetization in the interfacial region is not too surprising taking into account roughness and domain formation. More surprising is the fact that in contrast to cobalt, the much thinner iron layers do not lose magnetization, although their interfaces with chromium are also quite rough on the atomic scale. This controversy suggests that the main reason for interfacial roughness, which affects the magnetization profile, is not due to exchange interaction randomized over the interfacial region, but rather due to a randomizing of the anisotropy distribution, which is quite strong in cobalt. Random anisotropy axes may dramatically reduce the interfacial magnetization, decomposing the ferromagnetic state in a set of small interfacial domains associated, however, with interfacial roughness. This scenario is confirmed by our off-specular scattering result (see Fig. 9).

C. As-prepared state

Finally, we turn to the description of the as-prepared state. According to the PNR results shown in Fig. 10, left panel, the as-prepared sample with a periodicity of 16 nm reveals a magnetic state, which is completely different from the other two cases, the saturated state and the state in the plateau region. All four reflectivities are shown: $R_{U/D, D/U}$. This is important because in the as-grown state a noncollinear orientation of the magnetization vectors is manifested. Indeed, the reflectivity curves are characterized by additional half-order peaks. These indicate a magnetic doubling of the chemical unit cell. As already alluded to before, a simple antiparallel or antiferromagnetic orientation of the magnetic layers cannot explain the appearance of half-order peaks because the chemical unit cell already comprises two magnetic layers. Thus irrespective of any collinear magnetic orientation of these two layers, the magnetic Bragg peaks will always overlap in the position with the Bragg reflections from the chemical periodicity, if their periodicities are the same. Half-order peaks can only be explained if the magnetic unit cell consists of two chemical unit cells, i.e., $\text{Cr/Co}_1/\text{Cr/Fe}_1/\text{Cr/Co}_2/\text{Cr/Fe}_2$. By applying a magnetic field of 50 mT, for which the Fe layers are already in saturation, a big change of the half-order peak intensities can be recognized, but they do not disappear, as can be seen in the inset of the top panel in Fig. 10. Thus the Fe layers are now in a parallel state, but the Co layers in consecutive layers must still be in a noncollinear arrangement. The exact interpretation of the magnetization profiles comes from a fit to the data points, to be discussed later. However, on a more qualitative level, we can already recognize that the magnetization vectors of the Co layers must form an angle of about 45° with respect to the X and the Y axes, because the half-order Bragg reflections have roughly the same intensity in all four reflectivity channels.

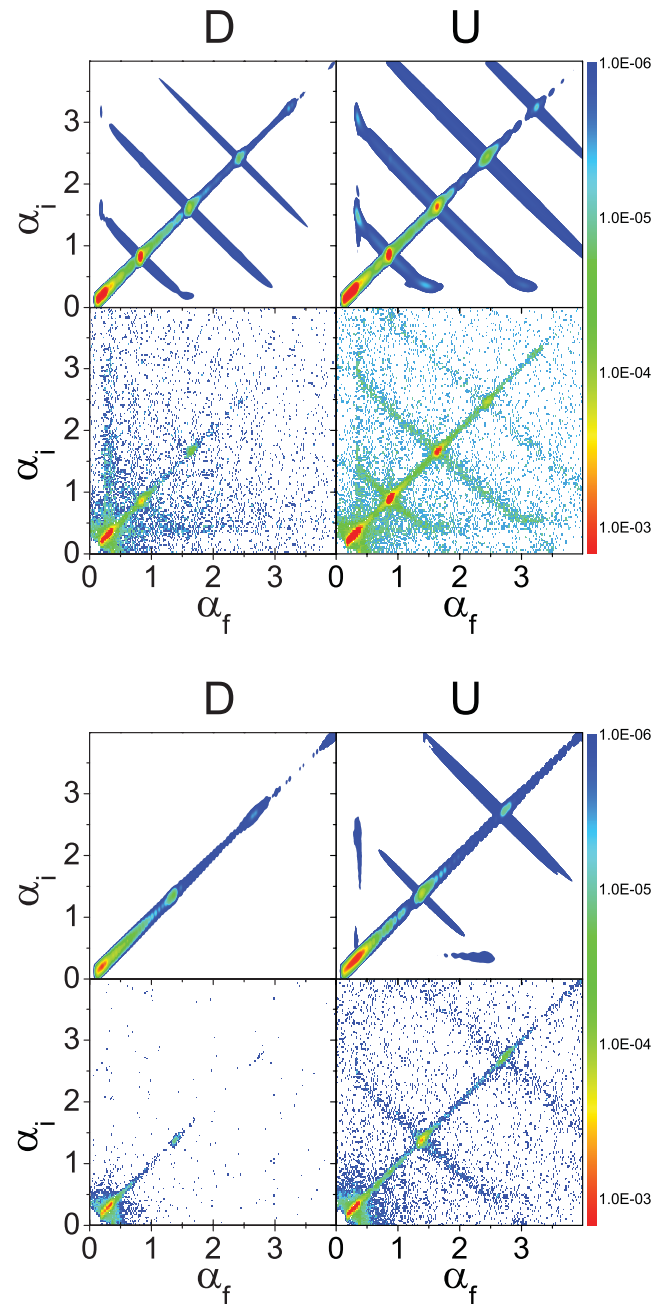


FIG. 9. (Color online) PNR maps of the 16-nm (top) and 10-nm (bottom) superlattices taken with an external magnetic field in the plateau region of the magnetic hysteresis. The incident neutrons are polarized either with spin up or with spin down. The incident and exit angles α_i and α_f , respectively, are given in degrees. For each case, the top rows show simulated maps from which the magnetic domain size can be inferred to be on the order of 30 nm.

In Fig. 10, bottom panel, we show the PNR results for the as-grown state of the 10-nm period sample. The solid lines are best fits to the data points and the corresponding SLD profiles for the Co and Fe layers are shown in the bottom right panel. It is very surprising that this superlattice does not show half-order peaks, indicating that the structural and the magnetic periodicities are identical. This is the case, although both superlattices were grown under the same conditions. However, the 10-nm superlattice has a magnetic layer thickness, which

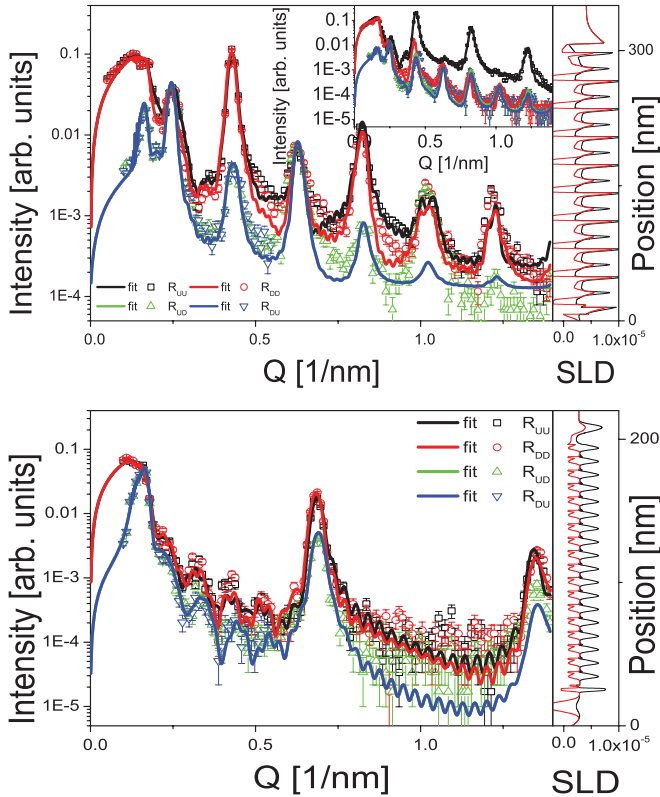


FIG. 10. (Color online) Polarized neutron reflectivity of the Co/Cr/Fe/Cr superlattices in the as-grown state. Top panel: sample with a periodicity of 16 nm. Bottom panel: sample with a periodicity of 10 nm. On the right hand side of both graphs, the scattering length density profiles for spin-up (black) and spin-down (red) neutrons are plotted.

is only half of the layer thicknesses in the 16-nm superlattice. Here, the domains do not arrange themselves in a configuration that doubles the periodicity as is the case for the thicker superlattice. We speculate that the decisive difference is the thickness of the Co layer, which when thin has a bcc structure and therefore a different crystal anisotropy than in thicker layers with hcp structure. We come back to this point in the discussion section. In passing, we want to note already here that the different magnetization configurations in the as-grown superlattices, noncollinear for 16 nm and collinear for 10 nm, was confirmed with a total of six additional [Fe/Cr/Co/Cr] superlattices, all showing the same behavior.

In Fig. 11, corresponding maps of the specular and diffuse intensity are shown for the as-grown state of the 10-nm Co/Cr/Fe/Cr superlattice, this time with polarization analysis, referred to as UU (up-up spins), DD (down-down spins), UD (up-down spins), and DU (down-up spins). The UD and DU maps are the spin-flip maps that originate solely from magnetic scattering of magnetic domains that deviate from the polarization axis of the incident neutrons. It is interesting to note that these spin-flip maps are quite symmetric with respect to the main diagonal apart of some asymmetry due to slightly different resolutions in angles of incidence and scattering. Such a symmetry is indicative of a domain state of the sample³⁷ with net magnetization close to zero.

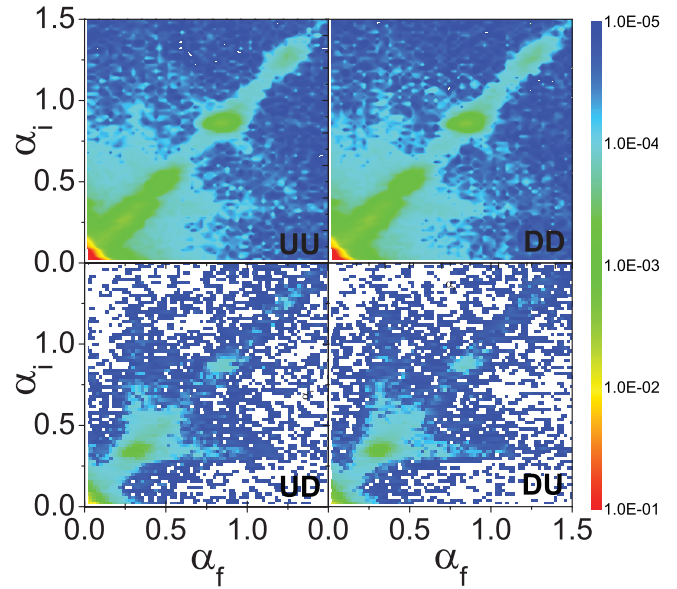


FIG. 11. (Color online) PNR maps of the 16-nm superlattice are shown in the as-grown state with polarization analysis. The top panels show the non-spin-flip maps, the bottom panels the spin-flip maps.

VI. PEEM STUDIES

PEEM with circular polarized incident x-rays tuned to the resonance edges of the respective element provides the possibility to investigate the magnetic domain structure in real space of samples with element selectivity and with a lateral resolution of a few nanometers.³⁸ Furthermore, the depth sensitivity of the response signal is such that only the first 10 nm can be probed. Therefore, in case of our superlattices, only the topmost layers are visible in the image. In all cases, the images are taken in the remanent as-grown state of the sample. For reference, we have first taken a PEEM image of a single Fe layer in the remanent state. In the left panel of Fig. 12, very large domains with extension on the order of 10 μm can be recognized, which are separated by 90° and 180° domain walls. The other two images show domain structures for the top layers in two samples with the layer sequence from top to bottom: Cr/Fe/Cr/Co/Cr (middle panel) and Cr/Co/Cr/Fe/Cr. These two samples are equivalent, but to recognize the finite penetration depth in PEEM, the top layer had to be exchanged in order to image the domain structure of Fe and Co, respectively. Otherwise, the layer thickness parameters correspond to those of the 16-nm superlattice. In both cases, an irregular domain structure with a domain size of much less than 0.5 μm can be seen. The irregularity and the domain size is typical for Co in this thickness range,³⁹ but it is very unusual for Fe. It appears that the existence of small Co domains in proximity to a Fe layer leads to a shrinkage of the Fe domains, which collapse to the same domain size as the one in the Co layer. A direct comparison of domain coupling was not possible because of the limited penetration depth of the resonant soft x rays. However, due to the same preparation methods used for both samples, the magnetic domain structure is supposed to be comparable.

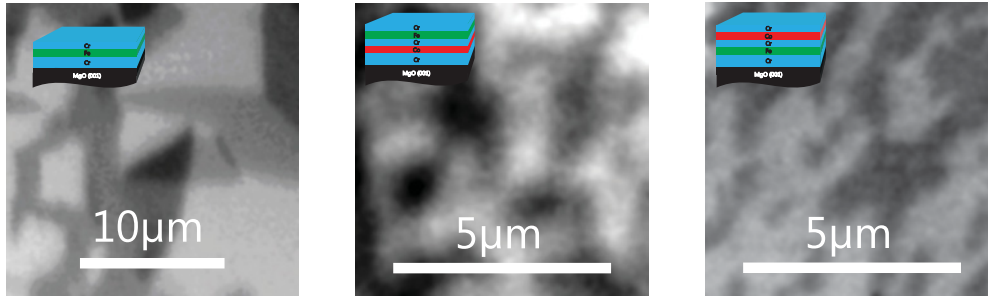


FIG. 12. (Color online) Fe domains in a pure Fe film (left), Fe domains in a Co/Cr/Fe sample (middle), and Co domains in a Fe/Cr/Co/Cr sample (right).

VII. DISCUSSION AND CONCLUSIONS

From all investigations presented so far, it is possible to propose a model for the domain structure in the as-grown state, which has the following features. First, we conclude that consecutive Fe layers are not aligned parallel to each other because of big changes that take place in the PNR intensities from the as-grown state to the state where Fe becomes saturated at 50 mT. Thus for this field value, the proper interpretation of the PNR spectrum also requires a noncollinear alignment of the Co layers but a parallel alignment of the Fe layers. Furthermore, the fact that the Bragg peaks also appear in the spin-flip channels indicates a rotation of the magnetization vectors with respect to the scattering plane. A possible model for the results in the as-grown state comprises two consecutive Fe layers aligned antiparallel to each other and two consecutive Co layers aligned also antiparallel to each other and with a tilt with respect to the Fe as shown schematically in Fig. 13(a). This spin structure explains the doubling of the magnetic periodicity over the chemical periodicity. By applying a field, first, the Fe layers rotate into the field direction [see Fig. 13(b)], and finally in the saturated state, both the Co and Fe layers are aligned ferromagnetically [see Fig. 13(c)]. On the return path, the Fe layers flip together into the antiparallel configuration

with respect to the Co layers, thereby eliminating the double periodicity [see Fig. 13(d)].

The simple spin structures sketched in Fig. 13 need to be modified as a result of the fitting of the PNR scans discussed before. In the as-grown state of the 16-nm sample, the Co layers are pairwise antiparallel ($\pm 90^\circ$). The Fe layers, in turn, are canted by 45° with respect to the Co layers, see Fig. 14(a). In a small field (50 mT), the Fe layers turn into the field direction, while the Co layers remain in the antiparallel orientation, see Fig. 14(b). In contrast, for superlattices with a periodicity of 10 nm and Co layer thicknesses of 2 nm, the doubling of the magnetic periodicity was never observed in the as-grown state. This was confirmed by three more superlattices with identical parameters. According to the best fit of the PNR scans, the spin structure in the as-grown state of the 10-nm superlattices is represented in Fig. 14(c), comprising parallel Co and Fe layers, which enclose an angle of about 90° between each other. This spin structure does not result in a doubling of the magnetic unit cell and therefore no half-order peaks are observed.

We argue that the differences observed for the 10-nm and 16-nm samples may be due to the martensitic phase transition of Co from bcc to hcp with increasing film thickness, which affects the magnetocrystalline anisotropy of Co. According to the epitaxial relation between Co and Fe described in Sec. III, for thick Co layers the Fe [100] axis (easy axis) is parallel to the

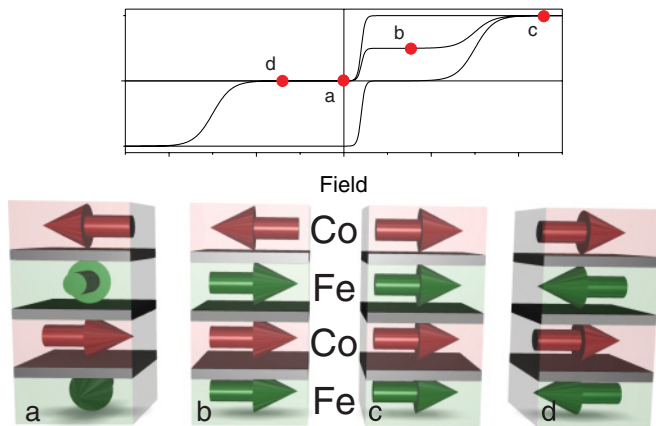


FIG. 13. (Color online) Magnetization in the Fe and Co layers: The top panel shows a schematic hysteresis including the initial magnetization curve. The red dots mark the positions for which the magnetization models in the lower panel are sketched: the spin spiral in as grown state (a), spin spiral in 50 mT (b), saturation (c), and antiparallel state (d).

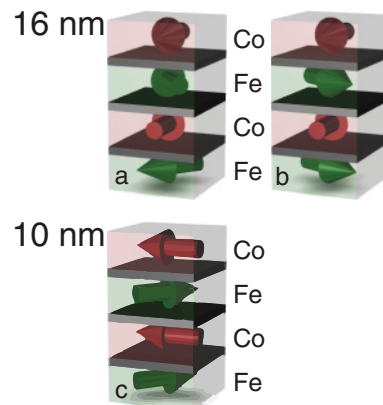


FIG. 14. (Color online) Top row: magnetization directions in the Fe and Co layers for the 16-nm sample in the as-grown state (a) and after applying a field of 50 mT (b). Bottom row: magnetization directions for the 10-nm sample (c) in the as-grown state.

hcp-Co [0001] axis (easy axis) and shows a fourfold symmetry because of the twinning of the Co layers on the Cr buffer and spacer layers. Another possible scenario would be a different domain structure that might form in the 10-nm and 16-nm superlattices. However, in order to discuss this possibility in more details, further PEEM and PNR investigations need to be done. During sample preparation, a local minimum for the spin structure is occupied that later cannot be reached anymore after applying a magnetic field. On the return path from saturation to the remnant state, neighboring layers arrange in a pairwise collinear antiparallel configuration. The noncollinear twisted state appears to have a potential barrier that makes this configuration unaccessible after a first saturation of the sample has been reached. But during evaporation of consecutive magnetic films, the as-grown state may settle into a state that minimizes the stray fields by a complete antiparallel alignment of the Fe and Co layers.

In summary, we have used the magneto-optic Kerr effect, polarized neutron reflectivity and polarized photoemission electron microscopy to analyze the spin structure and domain structure of asymmetric superlattices with a repeat unit [Fe/Cr/Co/Cr]. Thus the chemical unit cell is twice that of symmetric superlattices. The asymmetric superlattice is characterized by very different coercive fields for the Fe and Co layers, such that they switch at distinctly different field values. Between the coercive fields, the layer magnetization is pairwise collinear and antiparallel. This situation occurs for all studied [Fe/Cr/Co/Cr] superlattices, but not for one with a periodicity of 16 nm and a Co layer of 6 nm thickness.

In the latter superlattice, PNR measurements revealed in the as-grown state extra half-order Bragg peaks, indicating a doubling of the magnetic periodicity with respect to the chemical periodicity. This is clearly visible by comparing the specular reflectivity between saturation (Fig. 6) and the as-grown state, Fig. 10, where additional peaks along the specular reflectivity ridge appear. This state was only found for samples with Co layer thickness being mostly relaxed to the hcp phase. A possible explanation for these additional peaks is a noncollinear state where Fe and Co layers are parallel and twisted by an angle of 61° (66°) relative to their neighbors. Similar superlattices but with thinner Co layers, which are still in the bcc phase, do not show this effect. Thus we believe that the local magnetic anisotropy of bcc versus hcp Co in combination with local stray fields from the already deposited magnetic layers controls the noncollinearity in the as-grown state. The noncollinear state cannot be recovered after applying a magnetic field, but it can be reproduced with freshly grown superlattices. The noncollinear as-grown state is therefore a special metastable state that can only be reached during layer deposition.

ACKNOWLEDGMENTS

This work was supported by the Deutsche Forschungsgemeinschaft through SFB 491, by the BMBF under contracts 05ES3xBA/5 (BESSY, PEEM), by the HASYLAB at DESY Hamburg (Doris III W1.1, X-Ray), and by BMBF 05K10PC1 (Super ADAM reflectometer, ILL).

*Frank.A.Bruessing@ruhr-uni-bochum.de

†Theory Division, Petersburg Nuclear Physics Institute RAS, Gatchina, 188300 Russia.

¹Z. Celinski and B. Heinrich, *J. Magn. Magn. Mater.* **99**, L25 (1991); B. Heinrich, *Springer Tracts Mod. Phys.* **227**, 185 (2007).

²K. Efetov, I. A. Garifullin, A. F. Volkov, and K. Westerholt, *Springer Tracts Mod. Phys.* **227**, 251 (2007).

³J. E. Ortega and F. J. Himpsel, *Phys. Rev. Lett.* **69**, 844 (1992).

⁴E. Y. Tsymlal and D. G. Pettifor, *Perspectives of Giant Magnetoresistance*, edited by H. Ehrenreich and F. Spaepen, Solid State Physics Vol. 56 (Academic Press, London, 2001), pp. 113–237.

⁵I. K. Schuller, S. Kim, and C. Leighton, *J. Magn. Magn. Mater.* **200**, 571 (1999).

⁶C. F. Majkrzak, J. Kwo, M. Hong, Y. Yafet, D. Gibbs, C. L. Chien, and J. Bohr, *Adv. Phys.* **40**, 99 (1991).

⁷A. T. D. Grünwald, A. R. Wildes, W. Schmidt, E. V. Tartakovskaya, G. Nowak, K. Theis-Bröhl, and A. Schreyer, *Appl. Phys. Lett.* **96**, 192505 (2010).

⁸M. R. Fitzsimmons, B. J. Kirby, S. Roy, Zhi-Pan Li, I. V. Roshchin, S. K. Sinha, and I. K. Schuller, *Phys. Rev. B* **75**, 214412 (2007).

⁹M. Ahlberg, M. Marcellini, A. Taroni, G. Andersson, M. Wolff, and B. Hjörvarsson, *Phys. Rev. B* **81**, 214429 (2010).

¹⁰J.-B. Laloë, A. Ionescu, T. J. Hayward, J. Liiandro, J. A. C. Bland, and M. E. Vicker, *Appl. Phys. Lett.* **92**, 082505 (2008).

¹¹M. Buchmeier, R. Schreiber, D. E. Bürgler, and P. Grünberg, *Europhys. Lett.* **63**, 874 (2003).

¹²J. A. Borchers, J. A. Dura, J. Unguris, D. Tulchinsky, M. H. Kelley, C. F. Majkrzak, S. Y. Hsu, R. Loloee, W. P. Pratt Jr., and J. Bass, *Phys. Rev. Lett.* **82**, 2796 (1999).

¹³A. Bergmann, J. Grabis, B. P. Toperverg, V. Leiner, M. Wolff, H. Zabel, and K. Westerholt, *Phys. Rev. B* **72**, 214403 (2005).

¹⁴N. Wisner, S. Schatz, and B. J. Hickey, *Phys. Rev. B* **79**, 092408 (2009).

¹⁵K. Uchiyama, I. Ishida, E. Hirota, K. Hamada, and A. Okada, *J. Magn. Magn. Mater.* **156**, 427 (1996).

¹⁶B. C. Choi, A. Samad, C. A. F. Vaz, J. A. C. Bland, S. Langridge, and J. Penfold, *Appl. Phys. Lett.* **77**, 892 (2000).

¹⁷M. F. Toney, J. A. Borchers, K. V. O'Donovan, C. F. Majkrzak, D. T. Margulies, and E. E. Fullerton, *Appl. Phys. Lett.* **86**, 162506 (2005).

¹⁸K. Theis-Bröhl, R. Scheidt, Th. Zeidler, F. Schreiber, H. Zabel, Th. Mathieu, Ch. Mathieu, and B. Hillebrands, *Phys. Rev. B* **53**, 11613 (1996).

¹⁹F. Brüßing, G. Nowak, A. Schumann, S. Buschhorn, H. Zabel, and K. Theis-Bröhl, *J. Phys. D* **42**, 165001 (2009).

²⁰N. Metoki, W. Donner, and H. Zabel, *Phys. Rev. B* **49**, 17351 (1994).

²¹W. Donner, N. Metoki, A. Abromeit, and H. Zabel, *Phys. Rev. B* **48**, 14745 (1993).

²²A. Schreyer, R. Siebrecht, U. Englisch, U. Pietsch, and H. Zabel, *Physica B* **248**, 349 (1998).

- ²³M. Wolff, K. Zhernenkov, and H. Zabel, *Thin Solid Films* **515**, 5712 (2007).
- ²⁴A. Devishvili, K. Zhernenkov, B. P. Toperverg, B. Hjoevarsson, and H. Zabel (unpublished).
- ²⁵H. Dürr, T. Eimüller, H.-J. Elmer, S. Eisebitt, M. Farle, W. Kuch, F. Matthes, H.-C. Mertins, P. M. Oppeneer, L. Plucinski, C. M. Schneider, H. Wende, W. Wurth, and H. Zabel, *IEEE Trans. Magn.* **45**, 15 (2009).
- ²⁶P. Bödeker, A. Abromeit, K. Bröhl, P. Sonntag, N. Metoki, and H. Zabel, *Phys. Rev. B* **47**, 2353 (1993).
- ²⁷V. P. Romanov, S. V. Ulyanov, V. M. Uzdin, G. Nowak, M. Vadala, and H. Zabel, *J. Phys. D* **41**, 115401 (2008).
- ²⁸V. P. Romanov, S. V. Ulyanov, V. M. Uzdin, G. Nowak, K. Shokuie, and H. Zabel, *Phys. Rev. B* **82**, 165416 (2010).
- ²⁹P. Bödeker, A. Abromeit, K. Bröhl, P. Sonntag, N. Metoki, and H. Zabel, *Phys. Rev. B* **47**, 2353 (1993).
- ³⁰H. Kiessig, *Ann. Phys.* **10**, 769 (1931).
- ³¹The fitting software is available from Boris.Toperverg@RUB.de.
- ³²A. Y. Liu and D. J. Singh, *Phys. Rev. B* **47**, 8515 (1993).
- ³³A. Westphalen, M.-S. Lee, A. Remhof, and H. Zabel, *Rev. Sci. Instrum.* **78**, 121301 (2007).
- ³⁴C. F. Majkrzak, K. V. O'Donovan, and N. F. Berk, *Neutron Scattering from Magnetic Materials*, edited by Tapan Chatterji (Elsevier, Oxford, UK, 2008), p. 397.
- ³⁵B. P. Toperverg, *Polarized Neutron Scattering*, edited by Th. Brückel and W. Schweika, Matter and Materials Vol. 12 (Jülich: Forschungszentrum Jülich GmbH, Institut für Festkörperforschung, 2002), p. 274.
- ³⁶H. Zabel, K. Theis-Bröhl, and B. P. Toperverg, *The Handbook of Magnetism and Advanced Magnetic Materials, Vol. 3: Novel Techniques*, edited by H. Kronmüller and S. P. S. Parkin (Wiley, New York, 2007), pp. 1237–1307.
- ³⁷F. Radu, V. Leiner, K. Westerholt, H. Zabel, J. McCord, A. Vorobiev, J. Major, D. Jullien, H. Humblot, and F. Tasset, *J. Phys.: Condens. Matter* **17**, 1711 (2005).
- ³⁸H. A. Dürr and C. M. Schneider, *The Handbook of Magnetism and Advanced Magnetic Materials, Vol. 3: Novel Techniques*, edited by H. Kronmüller and S. P. S. Parkin (Wiley, New York, 2007), pp. 1367–1390.
- ³⁹J. McCord, R. Schäfer, R. Mattheis, and K. U. Barholz, *J. Appl. Phys.* **93**, 5491 (2003).